



**HAL**  
open science

# Three-Dimensional Structure and Dynamics of African Easterly Waves. Part I: Observations

George M. Kiladis, Chris D. Thorncroft, Nicholas M. J. Hall

► **To cite this version:**

George M. Kiladis, Chris D. Thorncroft, Nicholas M. J. Hall. Three-Dimensional Structure and Dynamics of African Easterly Waves. Part I: Observations. *Journal of the Atmospheric Sciences*, 2006, 63 (9), pp.2212 à 2230. 10.1175/JAS3741.1 . insu-00385797

**HAL Id: insu-00385797**

**<https://insu.hal.science/insu-00385797>**

Submitted on 9 Jun 2021

**HAL** is a multi-disciplinary open access archive for the deposit and dissemination of scientific research documents, whether they are published or not. The documents may come from teaching and research institutions in France or abroad, or from public or private research centers.

L'archive ouverte pluridisciplinaire **HAL**, est destinée au dépôt et à la diffusion de documents scientifiques de niveau recherche, publiés ou non, émanant des établissements d'enseignement et de recherche français ou étrangers, des laboratoires publics ou privés.

## Three-Dimensional Structure and Dynamics of African Easterly Waves. Part I: Observations

GEORGE N. KILADIS

*Earth System Research Laboratory, NOAA, Boulder, Colorado*

CHRIS D. THORNCROFT

*Department of Earth and Atmospheric Sciences, University at Albany, State University of New York, Albany, New York*

NICHOLAS M. J. HALL

*Laboratoire d'étude des Transferts en Hydrologie et Environnement, Grenoble, France*

(Manuscript received 3 June 2005, in final form 18 November 2005)

### ABSTRACT

The mean structure of African easterly waves (AEWs) over West Africa and the adjacent Atlantic is isolated by projecting dynamical fields from reanalysis and radiosonde data onto space-time-filtered satellite-derived outgoing longwave radiation. These results are compared with previous studies and an idealized modeling study in a companion paper, which provides evidence that the waves bear a close structural resemblance to the fastest-growing linear normal mode of the summertime basic-state flow over Africa. There is a significant evolution in the three-dimensional structure of AEWs as they propagate along 10°N across West Africa. At this latitude, convection occurs in northerly flow to the east of the Greenwich meridian, then shifts into the wave trough, and finally into southerly flow as the waves propagate offshore into the Atlantic ITCZ. In contrast, to the north of the African easterly jet along 15°N convection remains in southerly flow throughout the waves' trajectory. Along 10°N over West Africa, the location of convection is consistent with the adiabatic dynamical forcing implied by the advection of perturbation vorticity by the mean thermal wind in the zonal direction, as in the companion paper. Offshore, and along 15°N, the relationship between the convection and dynamics is more complex, and not as easily explained in terms of dynamical forcing alone.

### 1. Introduction

African easterly waves (AEWs) are the primary synoptic-scale disturbances affecting tropical northern Africa during the northern summer rainy season. Much has been written on AEWs since the pioneering studies of Carlson (1969), Frank (1969), and Burpee (1972, 1974, 1975), culminating in the extensive documentation coming out of the Global Atmospheric Research Program (GARP) Atlantic Tropical Experiment (GATE) field program over Africa and in the Atlantic ITCZ (Reed et al. 1977; Norquist et al. 1977; Nitta 1978; Thompson et al. 1979; Albignat and Reed 1980, and

many others). AEWs are rather similar in scale and structure to easterly waves along the Pacific Ocean ITCZ (e.g., Reed and Recker 1971), although there are distinct differences as well (Reed et al. 1977). It is now well established that AEWs serve as seed disturbances for hurricanes in the Atlantic ITCZ (Frank 1970; Avila and Pasch 1992; Landsea et al. 1998; Thorncroft and Hodges 2001), and AEW activity may be linked to changes in the numbers of Atlantic hurricanes and rainfall over Africa on interannual and longer time scales (e.g., Thorncroft and Hodges 2001; Hopsch et al. 2005, manuscript submitted to *J. Climate*), although this connection is still controversial.

Despite a relatively long history of research, there is still much to be learned about the dynamics and variability of AEWs, especially with regard to the role of convective coupling within the disturbances. Composite studies have shown strong links between AEWs and

---

*Corresponding author address:* George N. Kiladis, Earth System Research Laboratory, NOAA, 325 Broadway, Boulder, CO 80305-3328.

E-mail: george.kiladis@noaa.gov

rainfall (e.g., Reed et al. 1977; Thompson et al. 1979; Duvel 1990; Diedhiou et al. 1999; Gu et al. 2004) and also with Mesoscale Convective Systems (MCS; e.g., Payne and McGarry 1977; Machado et al. 1993; Fink and Reiner 2003). These studies suggest that the phasing between the lower-tropospheric trough axis of AEWs and the preferred location of MCSs varies quite substantially, depending on the region and the time of year (Gu et al. 2004). It appears that convection tends to be located to the west (ahead) of or within the trough over Africa, and east of the trough over the ocean, with convection more consistently located behind the trough north of the African easterly jet (AEJ) axis. A geographically dependent range of phasings is also seen in Pacific easterly waves (Reed and Recker 1971; Serra and Houze 2002; Petersen et al. 2003).

This study revisits the observed statistical structure of AEWs, in an effort to more thoroughly document their mean structure as a first step toward a better understanding of how convection is coupled to the waves. These structures will be compared with those from idealized modeling studies (e.g., Thorncroft and Hoskins 1994, hereafter TH94; Thorncroft 1995), which suggest that differences in the basic-state AEJ can influence the nature of AEWs that grow on them. Such differences are hypothesized to be due to changes in the basic-state wind shear, but other impacts may be due to the degree of coupling to convection, and perhaps the precise origin of the waves. A companion study (Hall et al. 2006, hereafter Part II) addresses whether the waves originate as the fastest-growing linear normal modes of the summertime basic-state flow over Africa, and the potential impact of the basic state on this growth. It will be shown in Part II that the spatial structure of such modes strongly resembles the observed structures isolated in this study, although their growth rates are weak, making it difficult to account for the presence of AEWs from modal growth alone.

## 2. Data and methodology

Much of the previous work on AEWs has used kinematic indices, such as 850- or 700-hPa meridional wind (e.g., Burpee 1974; Pytharoulis and Thorncroft 1999; Diedhiou et al. 1999; Gu et al. 2004) or relative vorticity (Reed et al. 1988; Céron and Guérémy 1999; Thorncroft and Hodges 2001; Hodges et al. 2003) to identify individual disturbances or as indices of wave activity. Here we take a somewhat different approach since we are interested in how convection is coupled to the disturbances and, ultimately, precipitation is the primary issue when considering the impact of AEW activity. This study will focus on those AEWs associated with

signals in satellite-derived outgoing longwave radiation (OLR), indicative of high cloudiness and thus deep convection. All of the main conclusions concerning the structure of AEWs are quite similar when using an appropriate kinematic predictor (such as filtered lower-tropospheric meridional wind) instead of filtered OLR.

AEWs coupled to convection can be effectively isolated through space–time filtering of OLR following the methodology of Wheeler and Kiladis (1999, hereafter WK99). In an extension of work by Takayabu (1994), WK99 showed through space–time spectral analysis of OLR that a significant fraction of tropical convection is organized into waves corresponding to the normal modes of the linearized shallow-water equations on an equatorial beta plane isolated by Matsuno (1966). WK99 also identified spectral peaks that did not correspond to these modes, such as the Madden–Julian oscillation (MJO; Madden and Julian 1994) and a peak during northern summer for less than six-day variability in westward-propagating zonal wavenumbers greater than six ( $\sim 7000$  km). This range has been referred to as the tropical depression or TD band in past studies (e.g., Takayabu and Nitta 1993). Figure 1 shows the June–August 1979–2003 spectrum of global OLR symmetric about the equator (i.e., of like sign at the same latitudes north and south of the equator) for  $15^{\circ}\text{S}$  to  $15^{\circ}\text{N}$ . It turns out that AEWs can be effectively identified by using a spectral filter centered on the wavenumber–frequency band of the prominent TD spectral peak shown in Fig. 1 (see Gu et al. 2003). Since easterly waves are primarily Northern Hemisphere disturbances, the antisymmetric spectrum (not shown) has a similar spectral peak (see Figs. 5c,d in WK99). Roundy and Frank (2004) show that TD-filtered variance over Africa peaks during northern summer.

Kinematic properties of the waves are obtained by projecting various dynamical parameters onto TD-filtered OLR at a given location (the base point) by means of a linear least squares regression technique. This approach has been used successfully in the past for isolating the dynamical structures of equatorial waves (e.g., Kiladis and Wheeler 1995; Wheeler et al. 2000), and is explained in detail in those studies. Briefly, dynamical fields and OLR (predictands) at each grid point on the globe are correlated and regressed against TD-filtered OLR at a base point over Africa to obtain a composite picture of AEW evolution. Results can be mapped for an arbitrarily chosen value of the predictor, and lag regressions can be used to examine their evolution. In this paper, the perturbations are scaled to a  $-40 \text{ W m}^2$  base point OLR anomaly at simultaneous lag (day 0), a typical minimum value seen locally during the

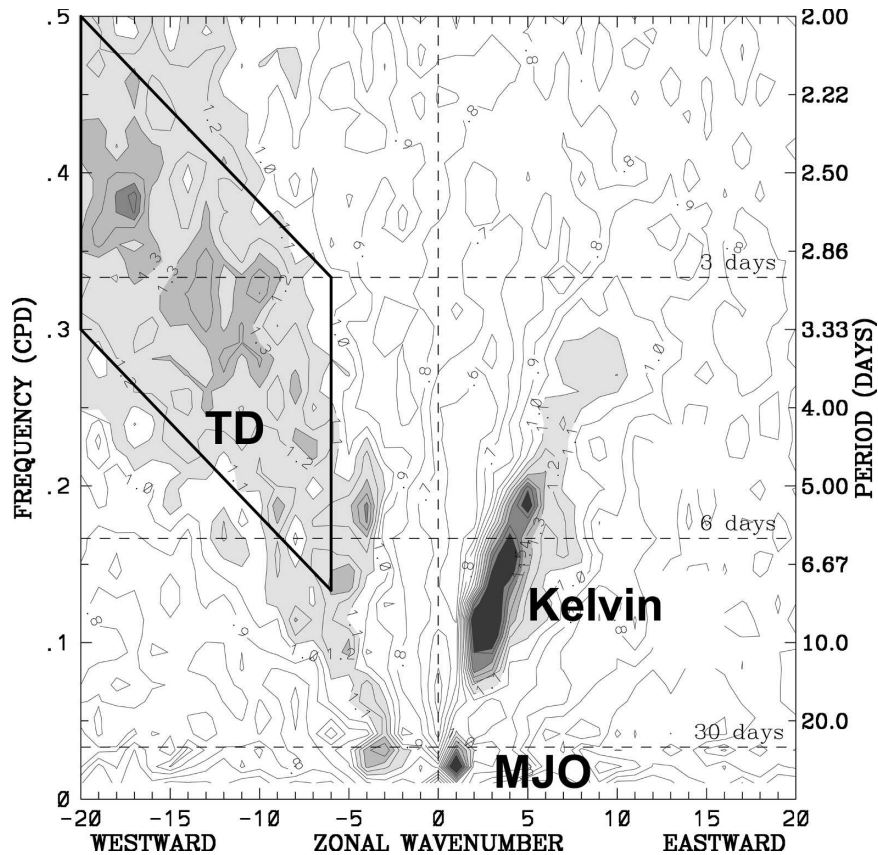


FIG. 1. Wavenumber–frequency power spectrum of the symmetric component of OLR for June–August 1979–2003, averaged from 15°N to 15°S, plotted as the ratio of the raw OLR spectrum against a smooth red noise background (see WK99 for details). Contour interval is 0.1. Shading begins at 1.1, where the signal is significant are greater than approximately the 95% level. Heavy solid box represents the region of TD wave filtering, and the spectral peaks of the MJO and Kelvin waves are also identified.

passage of a moderately strong AEW. The correlations are used to assess statistical significance using a standard  $t$  test once the degrees of freedom are determined from the autocorrelation characteristics of both the predictor and predictand. For much of what is presented here, dynamical parameters have been obtained from the European Centre for Medium-Range Weather Forecasts (ECMWF) 15-yr Re-Analysis (ERA-15), extending from 1979 to 1993. Previous studies have shown that gridded analysis products adequately represent the gross features of the structures of AEWs even on a case-by-case basis (Reed et al. 1988; Druryan et al. 1997; Diedhiou 1999), and that quantitative information is well represented statistically (e.g., Kiladis et al. 2005). The more recent ECMWF 40-yr Re-Analysis (ERA-40) was not readily available for this project, although we note that for horizontal structures, virtually identical results can be obtained using National Centers for Environmental Prediction–National Center for Atmo-

spheric Research (NCEP–NCAR) reanalyses products, lending confidence in the robustness of the results. As a further check, quality-controlled radiosonde observations of wind, temperature, and humidity from three African stations in the Comprehensive Aerological Reference Data Set (CARDS) are regressed against TD-filtered OLR at the nearest grid point to create time–height evolution plots. The vertical resolution of the reanalysis and radiosonde data is similar, with 11 or 12 mandatory pressure levels from 1000 to 100 hPa.

All of the results presented here are reproducible, in a slightly noisier form, by using <10 day (or <6 day) filtered OLR without any wavenumber filtering applied as a predictor instead of TD-filtered OLR. This indicates that the westward-propagating disturbances we identify account for the majority of the variance at <10 day periods. The advantage of using TD-filtered OLR is that it provides a more smoothly varying predictor, yielding a more continuous structure at lags, where ad-

ditional noise would tend to produce a less statistically significant signal.

A large selection of base points have been investigated, and we choose two of these as representative of the types of waves tied to convection over West Africa. One point is at  $10^{\circ}\text{N}$ ,  $10^{\circ}\text{W}$ , within the region of maximum mean African rainfall and convective variability, and the other at  $15^{\circ}\text{N}$ ,  $17.5^{\circ}\text{W}$  lies north of the AEJ axis within the region of maximum kinematic wave activity. As anticipated above, there are substantial differences in the structures of AEWs between these two regions.

### 3. Climatological background

Details of the climatological conditions over Africa and the adjacent tropical Atlantic have been treated in many previous studies (e.g., TH94; Fyfe 1999; Thorncroft and Blackburn 1999; Grist and Nicholson 2001; Fink et al. 2004), and so here we only briefly discuss aspects of synoptic-scale variability of relevance to AEWs. Figure 2a shows the climatological 700-hPa zonal wind during July–August 1979–93 from ERA-15, along with the mean OLR for the same period. As implied by the regions of lowest OLR, mean convection appears strongest over west-central Africa along  $7.5^{\circ}\text{N}$ , with local maxima over high terrain in Ethiopia, Cameroon, and along the coast of Guinea. At 700 hPa, the AEJ is nearly zonally oriented over the Atlantic close to  $15^{\circ}\text{N}$ , then there is a distinct break over West Africa, where the jet trends southeastward then eastward along  $10^{\circ}\text{N}$  toward Ethiopia. Below 700 hPa, the jet weakens and gives way to mean westerly flow at the lowest levels over West Africa (Fig. 1c in Part II; Grist and Nicholson 2001). In addition the core of the AEJ slopes upward to the east from around 700 hPa over the central Atlantic to just below 500 hPa over east Africa (see Fig. 1b in Part II).

The variability of synoptic-scale convective activity is represented in Fig. 2b by the daily standard deviation of less than 10-day-filtered OLR. Over most of the domain shown this band accounts for well over 80% of the submonthly (i.e., less than 30 day) OLR variability (Mekonnen et al. 2006). The level of synoptic-scale convective activity remains fairly steady across most of Africa until Ethiopia, where it drops off rapidly, even though mean convection is at a local maximum over the Ethiopian highlands. In the Atlantic, maximum OLR variability is collocated with the mean position of the ITCZ (along  $7.5^{\circ}\text{N}$ ), but at the coast of Africa this shifts abruptly to around  $12.5^{\circ}\text{N}$ , substantially poleward of the latitude of maximum mean deep convection. Thus synoptic-scale activity tends to excite convective activity to the north of its time-averaged position over the

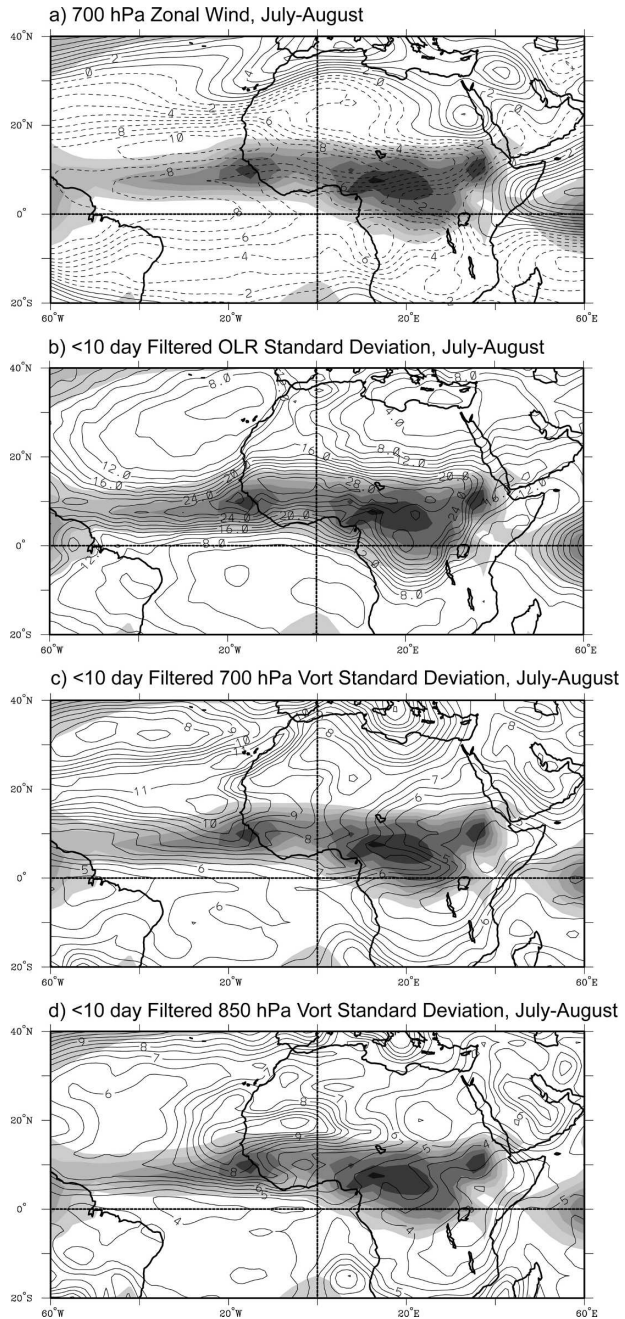


FIG. 2. July–August 1979–93 climatological OLR and (a) 700-hPa zonal wind, (b) daily std dev of <10 day filtered OLR, (c) daily std dev of <10 day filtered 700-hPa vorticity, and (d) daily std dev of <10 day filtered 850-hPa vorticity. Shading denotes OLR less starting at less than  $260 \text{ W m}^{-2}$ , at intervals of  $10 \text{ W m}^{-2}$ . Contour interval is  $1 \text{ m s}^{-1}$  in (a),  $2 \text{ W}^2 \text{ m}^{-4}$  in (b), and  $0.5 \times 10^5 \text{ m}^2 \text{ s}^{-1}$  in (c) and (d).

continent, while over the Atlantic it alternately reinforces or weakens the ITCZ along its mean axis. It has been suggested that westward-propagating 6–9-day disturbances also affect West Africa (Viltard et al. 1997;

Diedhiou et al. 1999), although maps of less-than-10-day-filtered and TD-filtered OLR both display the same general patterns as in Fig. 2b with slightly reduced amplitudes (not shown), implying that AEWs are the primary contributor to these signals.

Substantial evidence has been found for the presence of parallel tracks in AEW activity on either side of the AEJ, that appear to merge over the Atlantic (e.g., Reed et al. 1977; Nitta et al. 1985; Thorncroft and Hodges 2001; Hodges et al. 2003; Fink and Reiner 2003). Pytharoulis and Thorncroft (1999), and Céron and Guérémy (1999) suggest that waves in these two regions have different scales and structures, with the southern track more associated with convection but the northern track showing larger values of kinematic wave activity. In Figs. 2c,d the standard deviations of less-than-10-day 700- and 850-hPa vorticity show maxima in energy extending from West Africa into the Atlantic along 17.5°N. At 700 hPa, a diffuse track extends much farther out into the Atlantic, while the more localized activity at 850 hPa extends farther eastward across the Greenwich meridian. At both levels there is a hint of another axis of maximum activity extending southeastward along the West African coast and then inland toward the Congo, just north of the equator (also shown in Diedhiou et al. 1999). At 850 hPa, the main track extends just to the south of the Ethiopian Highlands, gradually weakening along the way. We note that this measure of variability peaks well north of the axis of peak OLR activity at all longitudes, confirming the results of several previous studies that found strong but relatively dry wave activity at latitudes along the southern fringe of the Sahara. It is also known that there can be strong coherence between individual waves in each track (e.g., Carlson 1969; Pytharoulis and Thorncroft 1999; Céron and Guérémy 1999).

#### 4. Horizontal structure

Figure 3 shows the horizontal structure of the 850-hPa circulation projected onto TD-filtered OLR at the base point (10°N, 10°W), located just north of the Guinea Highlands. This is just south of the mean AEJ axis and the region of maximum synoptic-scale OLR activity in Fig. 2b. The day-0 pattern (Fig. 3c) shows the convective signal located in phase with but just to the north of the center of a perturbation cyclone. The spatial extent of statistically significant OLR perturbations less than  $-10 \text{ W m}^{-2}$  covers an extensive area over and to the east of the Guinea Highlands north to around 15°N, extending to the southwest into the Atlantic ITCZ. Although detailed contour plots show that the OLR signal varies smoothly, this is a result of the av-

eraging over a large sample of cases, and in individual events the finer, mesoscale structure of the convective envelope becomes dominant (e.g., Berry and Thorncroft 2005). Flanking the convective signal are two regions of suppressed convection on either side, with an anomalous anticyclonic circulation to the east of Greenwich.

The evolution of the AEW signal from day  $-4$  through day  $+4$  is shown in Figs. 3a–e. A statistically significant convective center corresponding to the signal in Fig. 3c is first detected on day  $-4$  over Sudan at around 10°N, 30°E (Fig. 3a), but only a weak circulation exists at this time. An orographically favored genesis area for MCSs has been identified at around this location (e.g., Rowell and Milford 1993; Hodges and Thorncroft 1997; Mathon and Laurent 2001), in line with the notion that at least some waves could be triggered by this mechanism (Berry and Thorncroft 2005; Mekonnen et al. 2006). A significant circulation signal from the previous wave is seen near the Greenwich meridian, along with a couplet of OLR perturbations indicating enhanced convection near Greenwich, and suppressed convection to its east. Two days later the convective center originally located over Sudan has moved westward and is strengthening in a region typically associated with AEW amplification (e.g., Albignat and Reed 1980). Here convection is located in northerly perturbation flow, although it is displaced slightly toward the developing trough to its east.

The trough appears to catch up with the convection and becomes in phase with the OLR signal on day 0. This accelerated propagation of the circulation pattern with respect to OLR continues into day  $+2$ , as the main convective center propagates off the coast (Fig. 3d). Statistically significant circulation signals now extend to almost 20°S into the South Atlantic. At this point the OLR signal has developed a distinct positive (southwest to northeast) tilt, so that the negative OLR perturbation begins to extend northeastward into the southerly flow behind the wave. By the time this convective center reaches 40°W out in the Atlantic ITCZ at day  $+4$  (Fig. 3e), it is located well within the southerlies, essentially in quadrature with the vorticity field. This phase relationship continues to hold at later lags, as the convective center and associated wave propagate northwestward toward the Caribbean (not shown). Once the waves reach the longitudes of South America, their circulations are primarily confined to north of the equator (Fig. 3e).

We noted that in previous studies of AEWs, there was a wide range of reported phase relationships between the location of maximum convective activity and the trough axis. While some of this discrepancy might

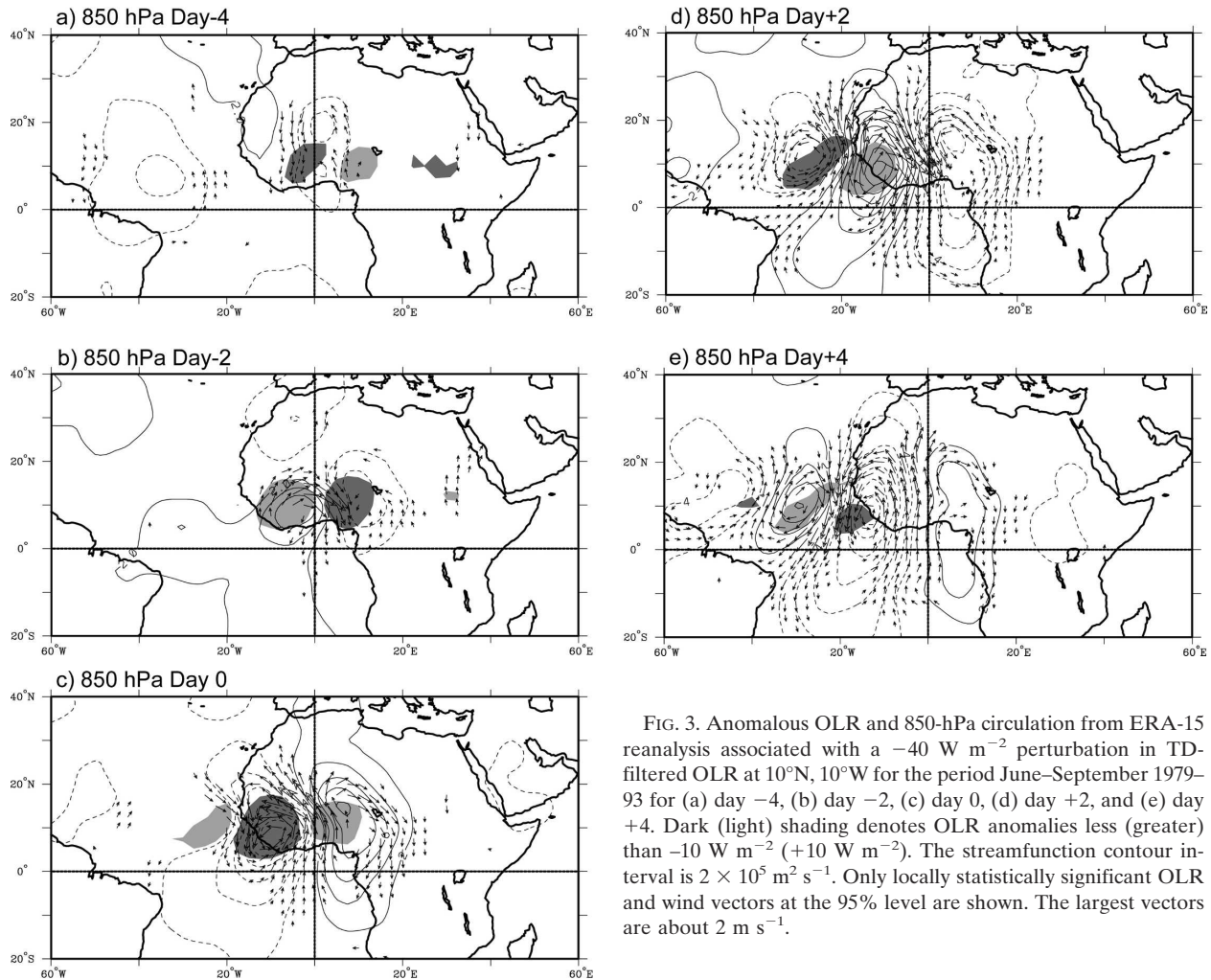


FIG. 3. Anomalous OLR and 850-hPa circulation from ERA-15 reanalysis associated with a  $-40 \text{ W m}^{-2}$  perturbation in TD-filtered OLR at  $10^\circ\text{N}, 10^\circ\text{W}$  for the period June–September 1979–93 for (a) day  $-4$ , (b) day  $-2$ , (c) day  $0$ , (d) day  $+2$ , and (e) day  $+4$ . Dark (light) shading denotes OLR anomalies less (greater) than  $-10 \text{ W m}^{-2}$  ( $+10 \text{ W m}^{-2}$ ). The streamfunction contour interval is  $2 \times 10^5 \text{ m}^2 \text{ s}^{-1}$ . Only locally statistically significant OLR and wind vectors at the 95% level are shown. The largest vectors are about  $2 \text{ m s}^{-1}$ .

be attributed to the short samples used, Fig. 3 shows a systematic shift within the composite wave from ahead of to behind the trough as the wave propagates across West Africa and into the Atlantic. However, this is not necessarily typical of waves at other latitudes. For example, while Fig. 3 is representative of AEWs propagating along  $10^\circ\text{N}$ , a subsequent negative OLR signal following the main wave appears in Fig. 3e at  $7.5^\circ\text{N}, 20^\circ\text{W}$ . In this case the convection is occurring in northerly flow within the Atlantic ITCZ, although it shifts closer into the trough at later lags (not shown). We also note that these OLR signals are generally in phase with the ERA-15 (and NCEP reanalysis) omega field (see below), implying a close relationship to precipitation.

The perturbation streamfunction fields in Fig. 3 display distinct horizontal tilts, positive to the south of the AEJ axis and negative to the north. As discussed further below and in Part II, these tilts indicate a flux of easterly momentum away from the jet, implying baro-

tropic energy conversions of zonal kinetic to eddy kinetic energy.

As seen in Fig. 3, the meridional extent of the disturbances is much larger than have been reported in the past, extending from well into the extratropics to south of the equator. This suggests the potential for tropical–extratropical interactions and also for equatorial mode influences. The wavelengths of the disturbances are around  $4000 \text{ km}$ , substantially larger than the  $2100\text{--}2800 \text{ km}$  seen in early studies (e.g., Carlson 1969; Burpee 1975; Reed et al. 1977) but more in line with what Diedhiou et al. (1999) found for waves along  $8^\circ\text{N}$ .

Based on time longitude diagrams (not shown), the OLR signals associated with AEWs along  $10^\circ\text{N}$  propagate westward at phase speeds of around  $11.5 \text{ m s}^{-1}$  to the east of Greenwich, but slow down to around  $8.5 \text{ m s}^{-1}$  by the time the waves reach the central Atlantic. However, if the meridional wind or vorticity is tracked, the phase speed over Africa is measured to be around

$12.5 \text{ m s}^{-1}$ , accounting for the changing phase relationships in Fig. 3, decreasing to a similar propagation speed of  $8.5 \text{ m s}^{-1}$  as the OLR signal over the Atlantic. As the waves move westward, their wavelengths also contract, resulting in a nearly constant period of about 4 days throughout their tracks. This decrease in wavelength over the Atlantic was also seen in the waves during GATE (e.g., Reed et al. 1977), and in NCEP reanalysis (Diedhiou et al. 1999). This contraction is also present in the normal mode analysis of Part II, suggesting a dynamical effect rather than one due to convective coupling.

As discussed above, several studies have noted pronounced differences in AEW structure on either side of the AEJ. As a comparison to the waves at  $10^\circ\text{N}$ , Fig. 4 displays the day  $-2$  to day  $+2$  evolution of OLR and circulation based on TD-filtered OLR at the base point ( $15^\circ\text{N}$ ,  $17.5^\circ\text{W}$ ). This point is located near Dakar, Senegal, along the coast of West Africa, well north of the region of strongest mean convection in Fig. 2a, and also just north of the latitude of strongest synoptic-scale OLR variability in Fig. 2b. In contrast to the disturbances farther south in Fig. 3, the convective signal in Fig. 4 remains in southerly perturbation flow throughout the life cycle of the wave at all lags, even as the waves are amplifying farther east (not shown). This is consistent with early observations of AEWs to the north of the AEJ, where maximum rainfall and thunderstorm frequencies are typically observed to the east of the trough (e.g., Burpee 1974; Gu et al. 2004). Over West Africa the perturbation vorticity maxima track somewhat to the north of the convection signal, along  $17.5^\circ\text{N}$  within the axis of maximum synoptic-scale kinematic activity in Fig. 2. Once off the coast, the circulations shift southward, following the main 850-hPa activity track in Fig. 2d. There is also a signal of secondary, southern vorticity track shown in Fig. 2d from the Congo, which then merges over the Atlantic, clearly visible in Fig. 4c.

The scale of the waves in Fig. 4 are close to that observed during early studies (e.g., Fig. 4c compares favorably with Fig. 1a in Reed et al. 1977), although there are still some interesting differences. Over Africa they propagate at close to  $9 \text{ m s}^{-1}$ , with a wavelength in the range of 3600 km and a period of 4.8 days. The wavelengths contract to 3000 km and their phase speeds slow to closer to  $7.5 \text{ m s}^{-1}$  over the Atlantic, giving nearly the same period as over the continent. Unlike the waves farther south, the OLR signals in Fig. 4 propagate at nearly the same phase speed as the dynamical signals. These waves still have horizontal tilts in the same sense as the waves farther south, although these are less pronounced to the north of the jet.

## 5. Vertical structure in reanalysis

AEWs that are coupled to convection have a deep vertical structure, with significant perturbations extending up to the tropopause. The 200-hPa circulation associated with convection at  $10^\circ\text{N}$ ,  $10^\circ\text{W}$  on day 0 (Fig. 5a) is broadly opposite to the 850-hPa pattern (Fig. 3c), with convection displaced slightly to the east of the center of an anticyclone and northerlies aloft. A large portion of these northerlies is divergent outflow from the convection, resulting in substantial perturbation flow across the equator. Unlike the lower-tropospheric evolution in Fig. 3, however, there is much less phase shift of the convective region with respect to the meridional wind over time, with convection remaining in northerlies as the wave evolves (not shown). This results in distinct changes in the vertical tilts of AEWs along  $10^\circ\text{N}$  as they propagate from the continent out over the Atlantic.

The corresponding 200-hPa flow for the  $15^\circ\text{N}$  base point (Fig. 5b) shows a more pronounced horizontally tilted pattern than for the waves farther south, resulting in a substantial upper-tropospheric poleward flux of westerly momentum (as shown below in section 6). In this case the OLR signal appears along the anticyclonic ridge throughout the wave's life cycle, and a comparison with Fig. 4b suggests a westward and poleward tilt of the vorticity field with height, although the vertical structure is more complicated as shown next.

### a. Meridional wind

Figure 6 shows longitude–height cross sections of meridional wind along  $10^\circ\text{N}$  corresponding to Figs. 3b–d and 5a. The first baroclinic structure seen here is very similar to Fig. 8a in Reed et al. (1977), with slightly westward-tilted meridional wind maxima up to about 300 hPa, and opposite flow above. The evolving relationship between the locations of the OLR minimum, vertical motion (to be shown below) and meridional flow is quite obvious as the region of implied convection shifts from deep northerly anomalies on day  $-2$  (Fig. 6a) to the trough on day 0 (Fig. 6b) and then into deep anomalous southerly flow by day  $+2$  (Fig. 6c). In earlier studies convection was shifted toward the northerly flow to the west of the trough (e.g., Figs. 9–11 in Reed et al. 1977), although Burpee (1975) showed a more complex pattern of vertical motion at 600 hPa in a combined Africa/Atlantic composite of GATE waves (his Fig. 4a), which peaked anywhere from the trough to the ridge depending on latitude. While these earlier studies reported that the level of maximum meridional wind perturbation occurs at around 700 hPa, in Fig. 6 the peak appears to steadily



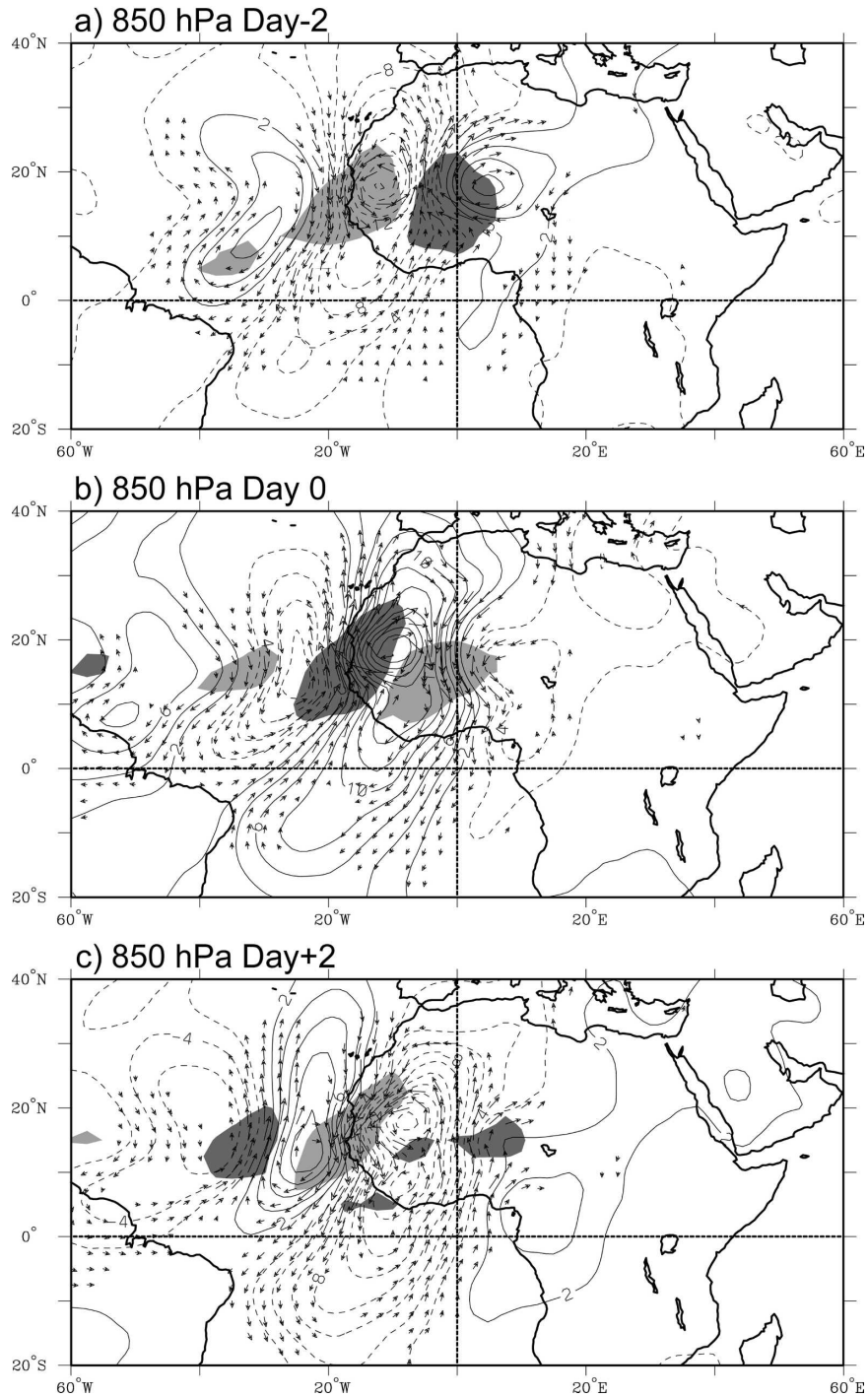


FIG. 4. As in Fig. 3 except for the point 15°N, 17.5°W on (a) day -2, (b) day 0, and (c) day +2.

lift from the lower troposphere over Africa up to 500 hPa over the Atlantic.

The meridional wind structure for the base point 15°N, 17.5°W (corresponding to Figs. 4 and 5b) is shown in Fig. 7. This differs from the waves farther

south in Fig. 6, with pronounced upward and eastward tilts below 500 hPa and opposite tilts above. These pictures are similar to those displayed by Burpee (1974, 1975) for AEWs propagating over Dakar (close to the base point used here), with the implied deepest convec-

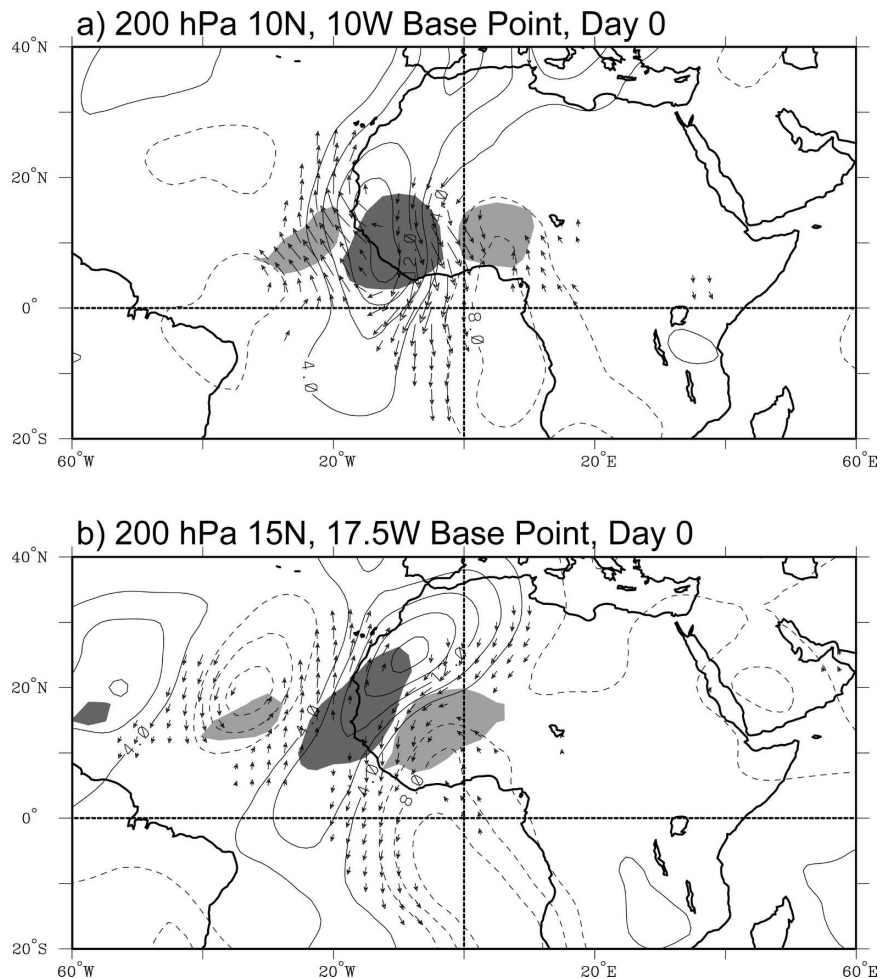


FIG. 5. As in Fig. 3 except for 200 hPa on day 0.

tion remaining in low-level southerlies. The vertical tilts in Fig. 7 are against the mean vertical shear of the AEJ, consistent with positive baroclinic energy conversions contributing to growth (TH94; Part II). As the wave propagates offshore, the southerly perturbation seen near Greenwich in Fig. 7a becomes oppositely tilted by the time it reaches 40°W six days later (Fig. 7c), implying a shift to a dominance of barotropic energy conversions over the Atlantic.

#### b. Divergence and vertical motion

Observed AEWs exhibit a complex divergence and vertical motion fields (Reed 1977; Thompson et al. 1979; Shapiro 1978; Jenkins and Cho 1991), with seemingly large differences in their structures between land and ocean regions (Duvel 1990). At the longitude of deepest convection along 10°N convergence peaks at 925 hPa and the strongest divergence at around 250 hPa on day 0, and a secondary divergence signal at 500 hPa

(Fig. 8a). This mass circulation is associated with a double maximum in omega (Fig. 9a), with peak upward velocity at 700 and 400 hPa. Results from the relatively short GATE sample were inconclusive, with some analyses indicating that the upper peak was more prevalent over land (Reed et al. 1977), perhaps as a result of deeper convection there, and that oceanic waves were dominated by the low-level peak at 700 hPa, as in reanalysis (Duvel 1990). However Thompson et al. (1979) also showed separate 700- and 350-hPa peaks using the final validated data from the oceanic GATE array centered on 8°N, 24°W. It was hypothesized that this structure originated from two populations of clouds, with the lower peak originating from shallow convection detraining at around 500 hPa, (as hinted at in Fig. 8a) and the upper-level peak corresponding to deep convection. Surprisingly, the lower peak in our analysis becomes much weaker and ultimately disappears as the AEWs propagate offshore,

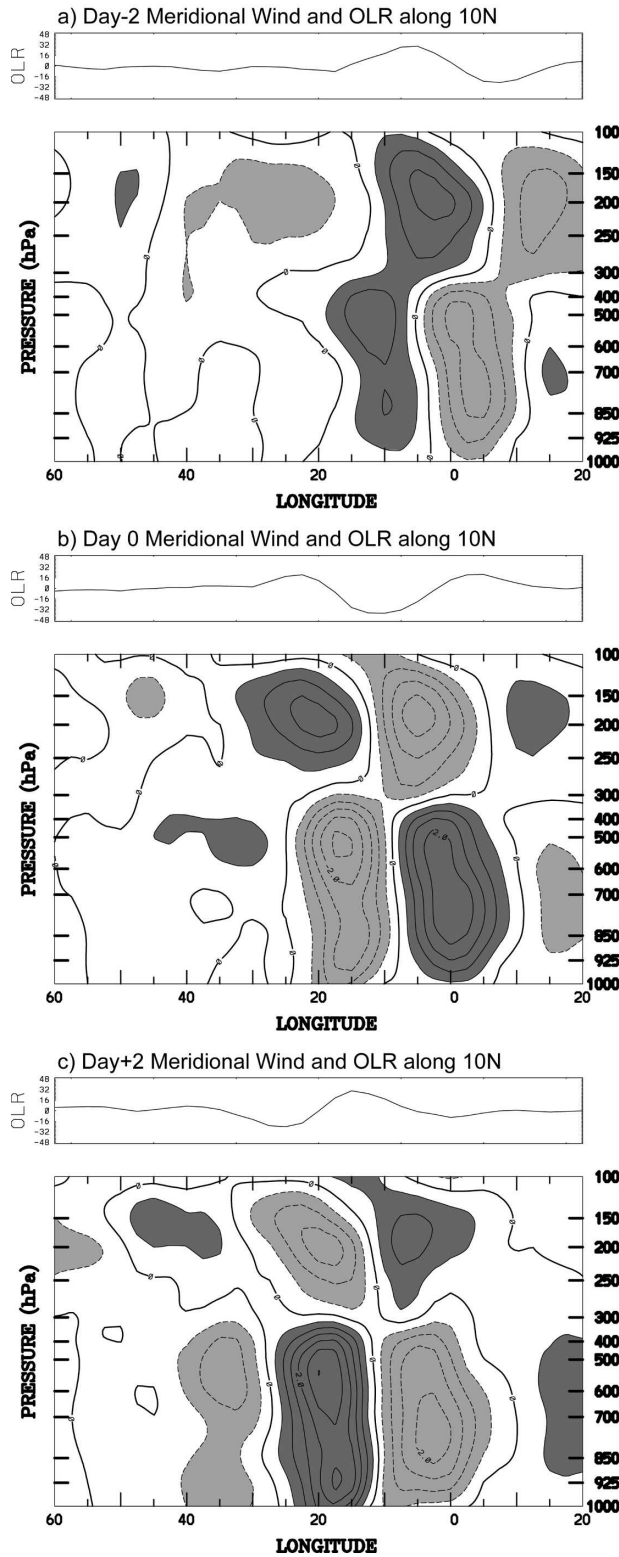


FIG. 6. Zonal-height cross section of anomalous meridional wind along 10°N associated with the pattern in Fig. 3 for (a) day -2, (b) day 0, and (c) day +2. Contour interval is 0.5 m s<sup>-1</sup>, negative contours dashed. Dark shading denotes anomalies greater than +0.5 m s<sup>-1</sup>, light shading less than -0.5 m s<sup>-1</sup>. The associated OLR anomaly along 10°N is shown at the top in W m<sup>-2</sup>.

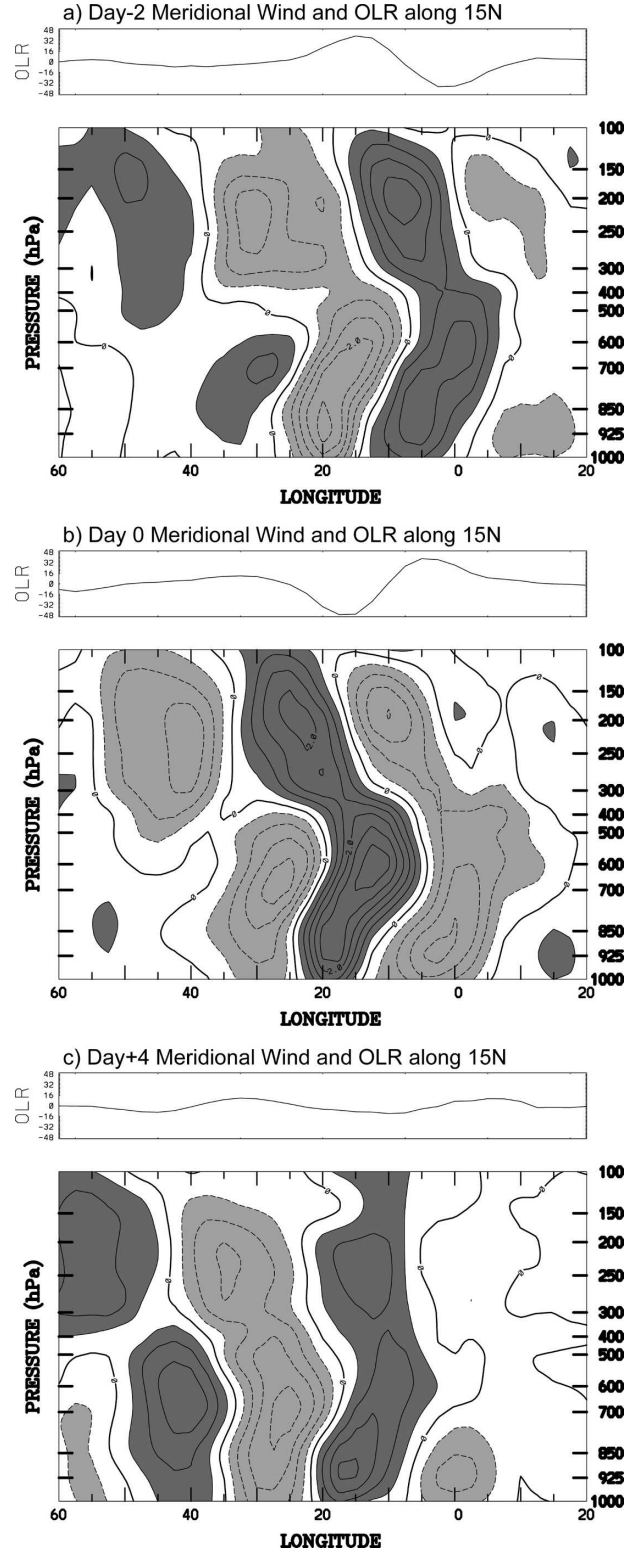


FIG. 7. As in Fig. 6, except along 15°N associated with the pattern in Fig. 4, for (a) day -2, (b) day 0, and (c) day +4.

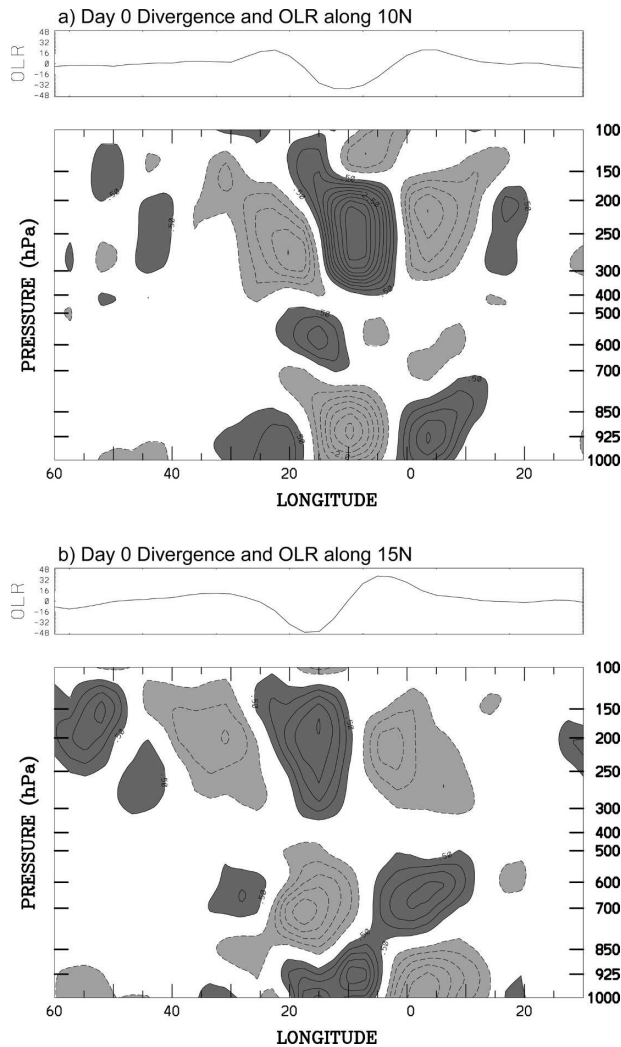


FIG. 8. As in Fig. 6, except for anomalous divergence on day 0 along (a)  $10^{\circ}\text{N}$  and (b)  $15^{\circ}\text{N}$ . Contour interval is  $0.5 \times 10^{-6} \text{ s}^{-1}$ . The associated OLR anomaly is shown along the top in  $\text{W m}^{-2}$ .

although they again become more prevalent for base points within the mid-Atlantic ITCZ along  $7.5^{\circ}\text{N}$  (not shown). This contrasts with easterly waves over the Pacific, which have a low-level convergence and upper-level divergence, leading to a peak in  $\omega$  at around the 300-hPa level (Reed and Recker 1977), as in other equatorial disturbances (e.g., Wheeler et al. 2000).

A much different mass circulation is implied for the  $15^{\circ}\text{N}$  base point, with the low-level convergence elevated to 700 hPa, and low-level divergence below this down to the surface (Fig. 8b). Figure 9b shows near-surface subsidence, with upward motion confined to above 600 hPa, but still peaking at 300 hPa. This signal persists for all grid points examined north of the AEJ axis over West Africa, and is reminiscent of the “checkerboard” vertical structure of the dry baroclinic normal

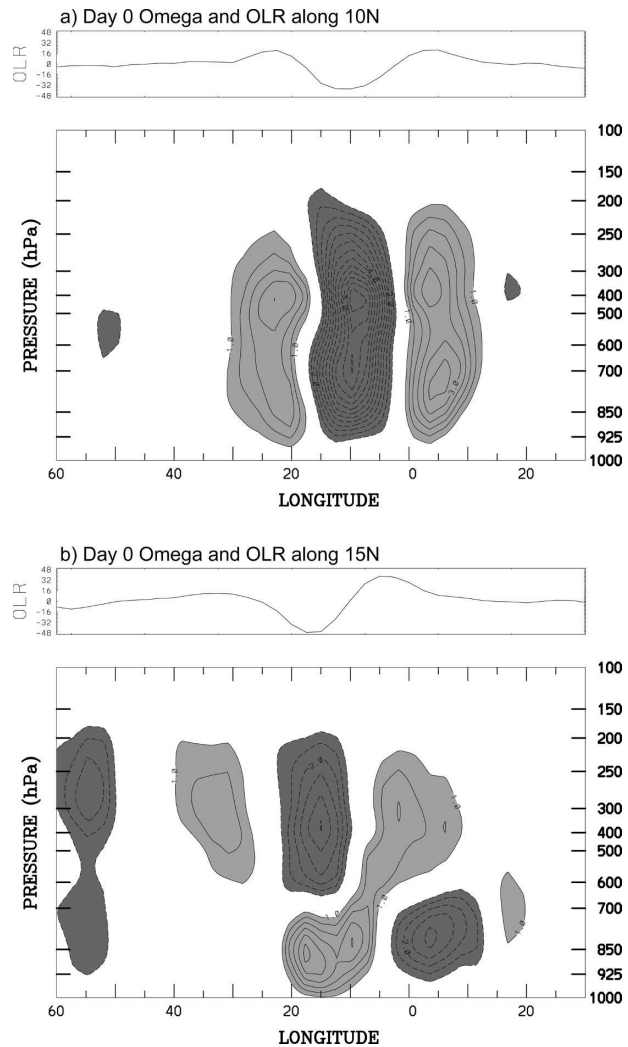


FIG. 9. As in Fig. 8, except for anomalous vertical motion  $\omega (= dp/dt)$ . Contour interval is  $1 \times 10^{-2} \text{ Pa s}^{-1}$ .

modes of TH94, who pointed out that a vorticity anomaly straddling a basic-state jet with opposite baroclinicity above and below gives rise to opposing vertical motion above and below (cf. Figs. 7b and 9b with Figs. 8b and 8c in TH94). The contrast with Fig. 9a suggests a fundamentally different interplay between convection and dynamics than is observed farther south. Consistent with TH94, and as discussed below, one origin of the low-level subsidence may be a combination of adiabatic forcing due to vorticity and temperature advection, although rain evaporation may also be a source as discussed further in section 6b below.

## 6. Vertical structure in radiosonde data

There are relatively few African radiosonde sites with sufficiently long records to examine the statistics

of AEW vertical structure as in Figs. 6 and 7. Fortunately, three stations with reliable and stable coverage are available over West Africa and they lie within the two regions examined above: Dakar (14.7°N, 17.5°W), Bamako (12.6°N 8.0°W), and Niamey (13.5°N, 2.2°W). Dakar is located close to the grid point that is the basis for Figs. 4 and 7, while Bamako is slightly west and north of the basis point for Figs. 3 and 6. The signals at Niamey are nearly indistinguishable from those at Bamako and so will not be shown here.

*a. Meridional wind*

Figure 10a shows a time–height section of meridional wind at Bamako regressed against TD-filtered OLR at the nearest grid point (12.5°N, 7.5°W). The structure of the meridional wind perturbations is very similar to those pictured in Fig. 6a, with the OLR minimum occurring in the trough axis between nearly vertically oriented meridional wind perturbations extending up to 300 hPa, and an abrupt reversal of the flow above that. As in Fig. 6a, there is an upper maximum at around 200 hPa, and the lower level maximum is initially at 500 hPa, but over time this descends to near the surface by day +4. This may be related to the fact that the wave is more tightly coupled to convection around day 0, when compared to the following disturbance (note the very weak OLR signal on day +3). Alternatively, this signal may be a manifestation of downward energy propagation, in line with baroclinic energy conversions and their associated Eliassen–Palm (EP) fluxes (e.g., TH94; Hsieh and Cook 2005). The meridional wind at Dakar (Fig. 10b) also compares well with the corresponding reanalysis result (Fig. 7a), with a much more strongly tilted structure than at Bamako.

*b. Temperature*

The regressed temperature evolution at Bamako with respect to TD-filtered OLR is shown in Fig. 11. Rather similar three-tiered tropospheric vertical structures were found by Reed et al. (1977) and Thompson et al. (1979) for AEWs during GATE, with temperature perturbations centered at 250–300 hPa flanked by opposite signed signals above and below. The temperature evolution is consistent with thermal wind balance as in the structure of dry normal modes (TH94), with, for example, a cold lower troposphere below the trough and warmth above it on day 0. This structure also compares well to other equatorial waves observed by Wheeler et al. (2000), Straub and Kiladis (2002), and Haertel and Kiladis (2004). As in those waves, surface AEW temperature is at a minimum following the passage of the convective signal, and convection and ver-

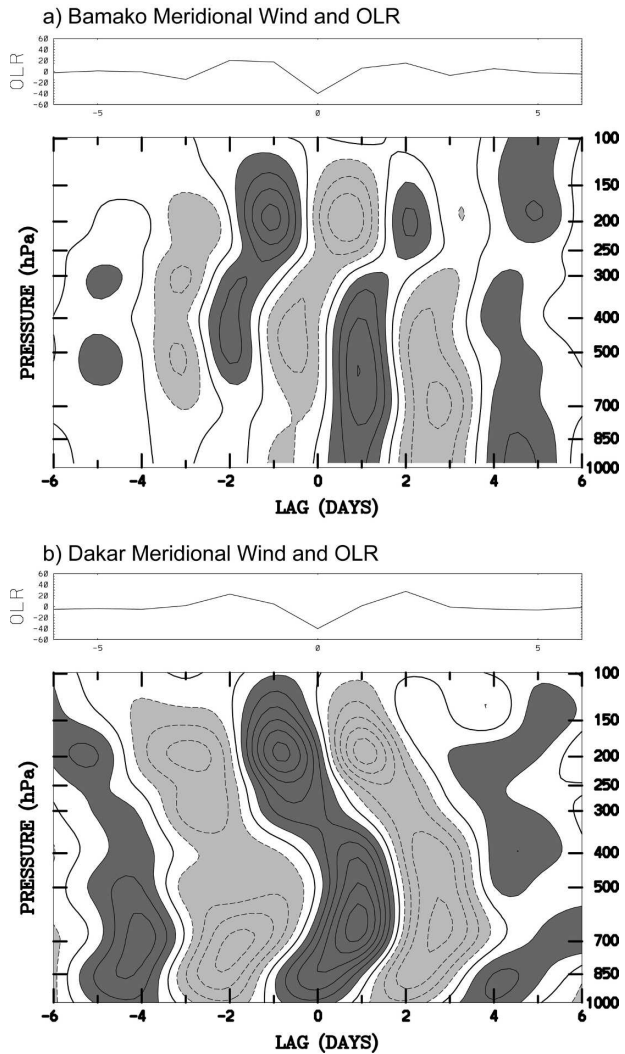


FIG. 10. Time–height cross section of the meridional wind anomaly at (a) Bamako and (b) Dakar, scaled to a  $-40 \text{ W m}^{-2}$  perturbation in TD-filtered OLR at the nearest grid point to each station. Contour interval is  $0.5 \text{ m s}^{-1}$ , negative contours dashed. Dark (light) shading denotes anomalies greater than (less than)  $0.5 \text{ m s}^{-1}$ . The associated OLR anomaly is shown at the top in  $\text{W m}^{-2}$ .

tical motion is in phase with a positive midtropospheric temperature perturbation, implying the conversion of available potential to kinetic energy. Missing from Fig. 11a, however, are the strong vertical tilts in the temperature structures of other equatorial waves seen in the studies cited above.

Unlike their wind structures, the Dakar temperature evolution (Fig. 11b) is similar in phasing to Bamako, with a midtropospheric temperature maximum overlain by a cold anomaly, but the low-level temperature perturbations are much larger. More strongly tilted perturbations aloft are also indicative of greater baroclinicity

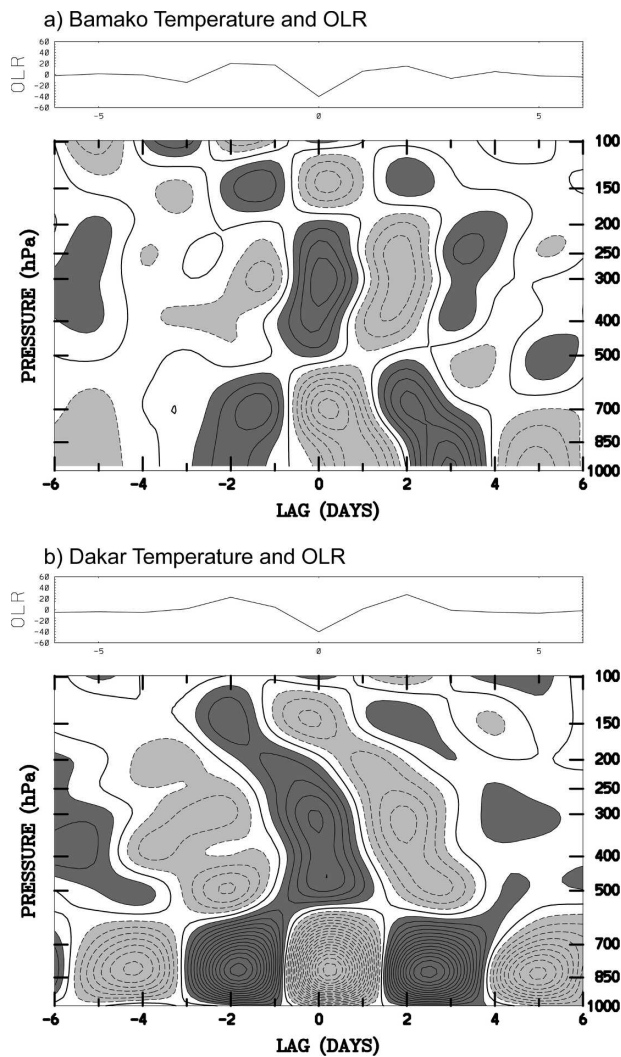


FIG. 11. As in Fig. 10, except for anomalous temperature at (a) Bamako and (b) Dakar. Contour interval is 0.1 K.

due to increased basic-state temperature gradients. Temperature advection appears to be a dominant factor at Dakar (Burpee 1974), where surface southerlies would advect relatively cool marine air (see Fig. 4b). However, strong evaporative cooling within squall lines is also an important factor at this latitude (e.g., Roca et al. 2005), and would also be accompanied by divergence and vertical motion structures similar to those in Figs. 8b and 9b (e.g., Lafore and Moncrieff 1989). Reconciliation of the precise diabatic versus adiabatic sources for these observed synoptic-scale signals will require further detailed budget and modeling studies.

### c. Specific humidity

The specific humidity evolution in Fig. 12a at Bamako differs markedly from composites by Reed et al.

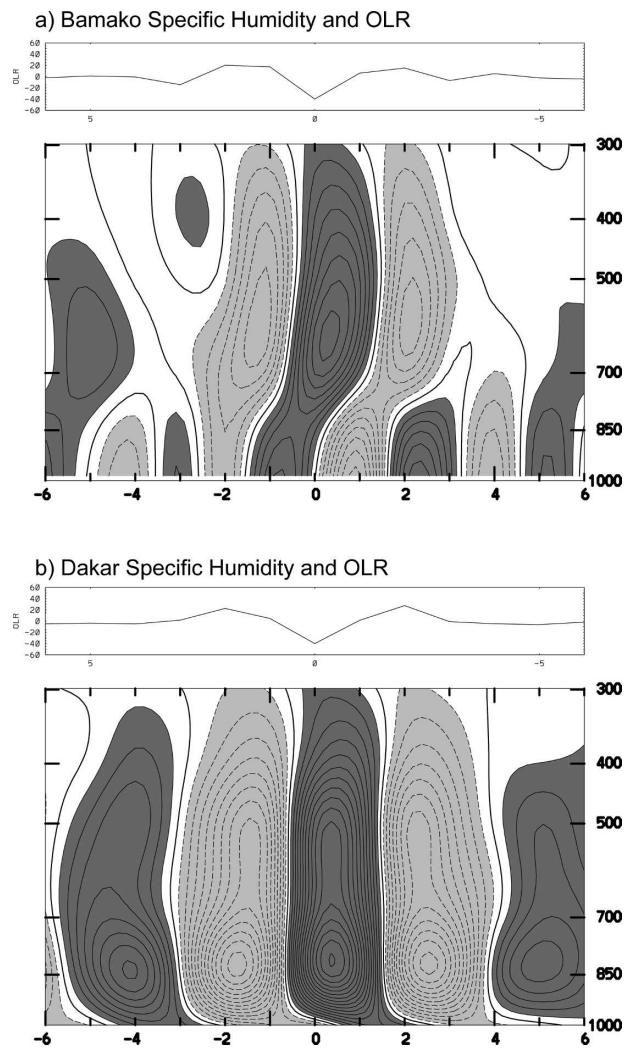


FIG. 12. As in Fig. 10, except for anomalous specific humidity at (a) Bamako and (b) Dakar. Contour interval is  $1 \times 10^{-1} g\ kg^{-1}$ .

(1977). Humidity is high ahead of the trough axis, in northerly flow, then, as the convective region passes, this moisture is lifted into the mid- and upper troposphere while drying occurs at low levels between day 0 and day +1. This evolution is consistent with a progression from shallow to deep convection, and then to stratiform precipitation as the wave passes. This is once again similar to observations of a wide variety of other equatorial disturbances across a wide range of scales, from GATE squall lines (e.g., Gamache and Houze 1985) on up to the MJO (e.g., Kiladis et al. 2005). Reed et al. (1977), however, show that humidity was highest after the trough passage, which they attributed to advection of moisture in southerly flow. This discrepancy is possibly due to Bamako's location compared to the GATE composite waves, south of the axis of highest

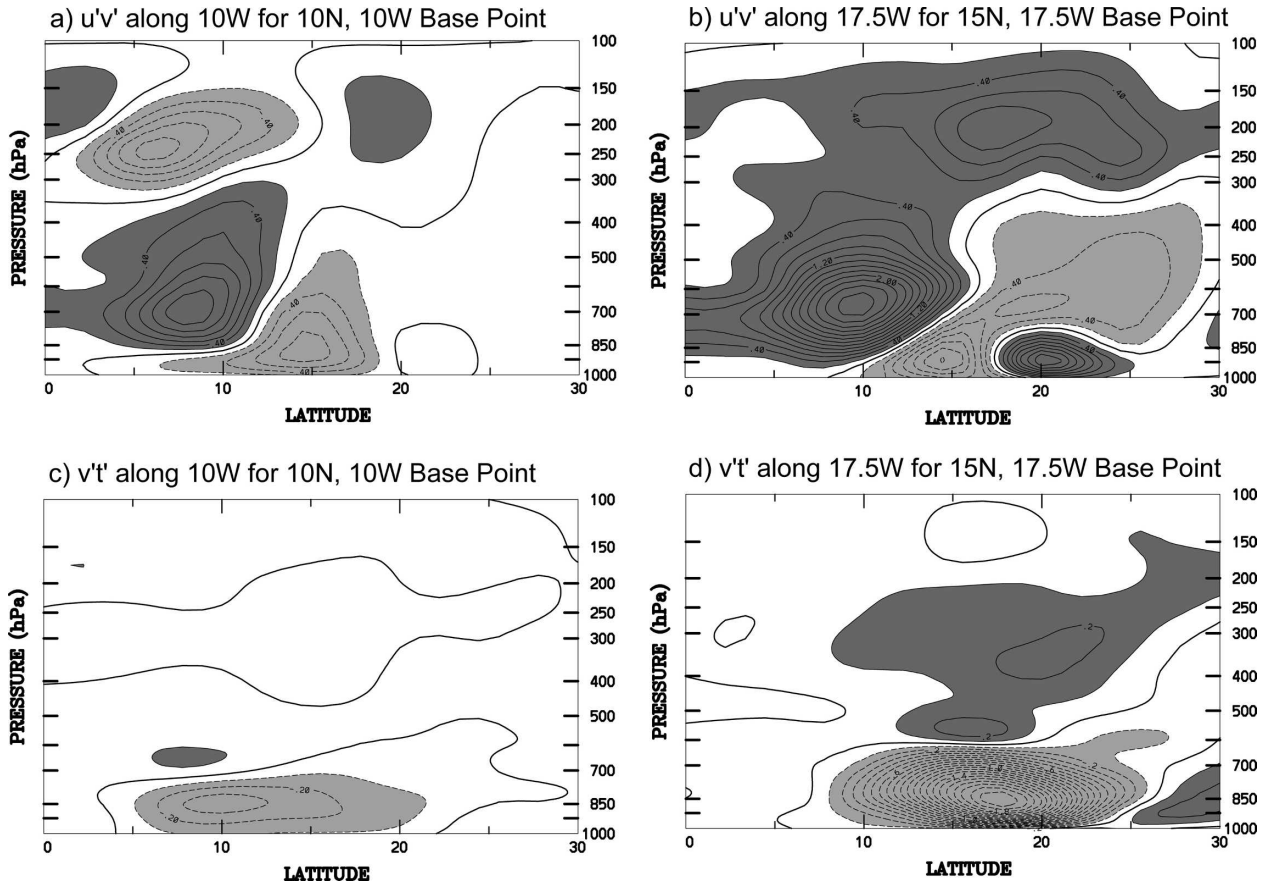


FIG. 13. Meridional–height cross sections of integrated covariances from day  $-4$  to day  $+4$  of (a)  $u'v'$  along  $10^\circ\text{W}$  for the base point shown in Fig. 3, (b)  $u'v'$  along  $17.5^\circ\text{W}$  for the base point shown in Fig. 4, (c)  $v'T'$  along  $10^\circ\text{W}$  for the base point shown in Fig. 3, (d)  $v'T'$  along  $17.5^\circ\text{W}$  for the base point shown in Fig. 4. Contour interval is (a), (b)  $0.2 \text{ m}^2 \text{ s}^{-2}$ , and (c), (d)  $0.1 \text{ K m s}^{-1}$ .

mean specific humidity at the surface near  $13^\circ\text{N}$  (see Hodges and Thorncroft 1997).

The Dakar specific humidity evolution (Fig. 12b) shows a more vertically stacked structure. This is perhaps an effect of the predominance of vertical transport in deep convection on the humidity profile rather than horizontal advection, except perhaps at the surface where there is a slightly drier than normal layer on day 0 in the relatively cold southerly flow implied by Figs. 10b and 11b.

### 7. Eddy fluxes and implied energetics

As in Burpee (1972, 1974), Norquist et al. (1977), and Part II, an assessment of the energetics of AEWs can be obtained from integrated covariances of perturbation terms. Figure 13 shows meridional cross sections of the results of these calculations for two second moment terms,  $u'v'$  and  $v'T'$ . These were obtained by calculating the product of the perturbation quantities from the regression results from day  $-4$  to day  $+4$ , over roughly

two full cycles of an AEW passage. Since this calculation includes just products between separately regressed perturbations, and not cross products that would be associated with the interaction between AEWs and other frequencies, it comprises only a portion of the impact of transient AEWs on the momentum or heat budget, although such terms are generally found to be small when the calculation is repeated and the products are taken first before the regression (not shown). Here we show the results of the former approach to provide a consistent comparison with the energetics calculations in Part II.

For both the  $10^\circ$  and  $15^\circ\text{N}$  base points, the flux divergence of easterly momentum (or convergence of westerly momentum, at a maximum near the zero line of Figs. 13a,b) within AEWs varies substantially and slopes northward and upward with height, acting to decelerate the easterlies from near the surface at  $10^\circ\text{N}$  up to around 600 hPa at  $15^\circ\text{N}$ . The peak in the flux divergence near jet level (700 hPa) is in general agreement with the budgets of Norquist et al. (1977), and the over-

all pattern is remarkably similar to that of the idealized waves in Part II.

The meridional temperature flux (Figs. 13c,d) show the expected downgradient transport, with a sign reversal at jet level, consistent with baroclinic growth. Large transports are noted in Fig. 13d, reflecting a larger temperature gradient and more baroclinicity at 15° than at 10°N. This is also manifested by less vertical tilt of the meridional wind in Fig. 6 versus Fig. 7, with barotropic conversions appearing to be more important than baroclinic conversions in the waves farther south, consistent with weaker baroclinicity and perhaps more important contributions from convective processes there (Reed et al. 1977; Norquist et al. 1977; Hsieh and Cook 2005). The overall structure of temperature transport concentrated below the jet is again consistent with Norquist et al. (1977) and shows excellent agreement with the normal modes of Part II.

### 8. Adiabatic forcing of vertical motion

A crucial question regarding the coupling between convection and equatorial waves concerns whether they originate as dry disturbances that then couple to convection, or whether convection initiates a circulation that then projects onto a preferred mode of atmospheric circulation. In the case of AEWs we are able to diagnose the dynamical (or adiabatic) contribution to the forcing due to the advection of vorticity and temperature through the use of  $\mathbf{Q}$  vectors (Hoskins et al. 1978), which neglects the diabatic forcing term of the omega equation. The  $\mathbf{Q}$  vectors are useful in the region of the AEJ, despite the fact that AEWs occur at a latitude where the original quasigeostrophic assumptions involved may not be valid.

We use a slightly modified version of the quasigeostrophic  $\mathbf{Q}$  vector (e.g., Holton 2004),

$$Q_1 \equiv -\frac{R}{p} \frac{\partial V_\psi}{\partial x} \nabla \cdot \mathbf{T} = -\frac{R}{p} \left( \frac{\partial u_\psi}{\partial x} \frac{\partial T}{\partial x} + \frac{\partial v_\psi}{\partial x} \frac{\partial T}{\partial y} \right), \quad (1)$$

$$Q_2 \equiv -\frac{R}{p} \frac{\partial V_\psi}{\partial y} \nabla \cdot \mathbf{T} = -\frac{R}{p} \left( \frac{\partial u_\psi}{\partial y} \frac{\partial T}{\partial x} + \frac{\partial v_\psi}{\partial y} \frac{\partial T}{\partial y} \right), \quad (2)$$

where the geostrophic wind is replaced by the nondivergent or rotational wind  $V_\psi$  (e.g., Davies-Jones 1991; Mallet et al. 1999). The vertical motion is proportional to  $\nabla \cdot \mathbf{Q}$  (Hoskins et al. 1978). In this study  $\mathbf{Q}$  vectors and their divergences are calculated through centered differencing of gridded reanalysis data (see the appendix).

The result of the 850-hPa level  $\mathbf{Q}$  vector regression for the 10°N base point is shown in Fig. 14. Superimposed on the  $\mathbf{Q}$  vectors and  $\nabla \cdot \mathbf{Q}$  is 850-hPa omega,

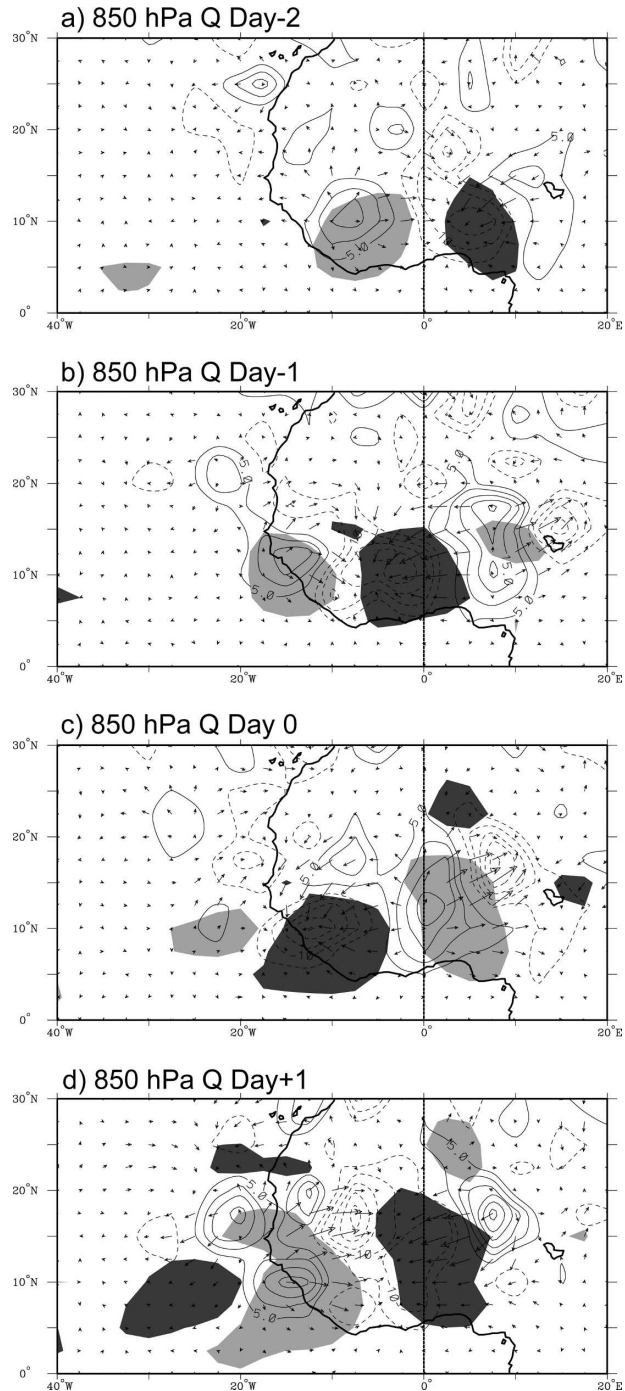


FIG. 14. Perturbation  $\mathbf{Q}$  vectors,  $\nabla \cdot \mathbf{Q}$  (contours), and 850-hPa omega (shading, dark negative, or upward). Contour interval is  $5 \times 10^{-19} \text{ Pa}^{-1} \text{ s}^{-3}$  and the largest vectors are around  $10 \times 10^{-14} \text{ m Pa}^{-1} \text{ s}^{-3}$ . Shading starts at  $\pm 1.2 \times 10^{-2} \text{ Pa s}^{-1}$ .

which matches up quite well with the OLR signals in Fig. 3. There is strong correspondence between the dynamically forced vertical motion at 850 hPa and deep convection for the day -2 through day +1 stages of the



AEW evolution along 10°N. Convergent  $\mathbf{Q}$  vectors slightly leading the regions of maxima in vertical velocity in Fig. 14 and corresponding OLR minima in Figs. 3b,c. This calculation includes all terms in Eqs. (1), (2), and (A3), but the perturbation vorticity advection by the mean thermal wind in the zonal direction accounts for an overwhelmingly large fraction of the forcing (see the appendix).

An examination of vertical cross sections of  $\nabla \cdot \mathbf{Q}$  (not shown) indicates moderate adiabatic forcing and vertical motion in the lower troposphere at the time of convective initiation (e.g., at 30°E in Fig. 3a), which then strengthens substantially as the wave approaches the region of the stronger AEJ and associated baroclinicity over West Africa. The slight phase lead of  $\nabla \cdot \mathbf{Q}$  compared to vertical motion and convection by around 1/8 of a cycle is also seen for other base regions over Africa, but differs from what is observed in the dry modes in Part II, where omega is in phase with  $\nabla \cdot \mathbf{Q}$ , as expected. This lag in observations may reflect the time it takes for convection to develop locally once forced, or may be related to more complex interactions with mesoscale features that are unresolvable through the methodology used here.

Positive vorticity advection still slightly leads the vertical motion as the convection begins to move into the 850-hPa trough in Figs. 14c,d. This appears to be due to a shift in the location of the perturbation zonal vorticity gradient in Eq. (A6), so that the phasing between the trough and convection is still dynamically consistent (see Part II). Shapiro (1978) and Jenkins and Cho (1991) also found that the vorticity balance of AEWs was nearly linear. However, in those studies the balance was dominated by advection of perturbation vorticity by the mean zonal wind, along with the advection of mean vorticity by the perturbation meridional wind plus the perturbation stretching term. The importance of stretching is not surprising, since their waves were accompanied by strong convective activity over the oceanic GATE array. This may explain why, as the waves move offshore, and for base points over the Atlantic ITCZ, the level of maximum adiabatic forcing weakens dramatically as depicted by  $\mathbf{Q}$  and rises to the 700-hPa level (not shown), even though the OLR signal still remains strong (as in Fig. 4). Off-equatorial convection in Atlantic AEWs within poleward flow suggests a Sverdrup balance between poleward advection of planetary vorticity and low-level convergence. This seems reasonable over the Atlantic since the wave phase speed decelerates to closer to the speed of the jet in Fig. 1a, resulting in a nearly stationary intrinsic phase speed at low levels.

Perhaps not surprisingly,  $\nabla \cdot \mathbf{Q}$  also does a poor job

in accounting for the more complicated vertical motion field for the 15°N, 17.5°W base point (not shown). This is in line with the likely important role of diabatic processes in the energetics of African easterly waves over some regions (Norquist et al. 1977; Hsieh and Cook 2005). In view of the remaining questions concerning the relationship between convection and circulation in these waves, detailed comparisons of the vorticity budgets and energetics of AEWs over West Africa versus the Atlantic and Pacific ITCZ seem warranted as a topic for future study.

## 9. Discussion

This study and Part II have highlighted the apparent strong dependence of AEWs on the peculiarities of the basic state and its baroclinicity over West Africa for their maintenance and growth. As shown in the previous section and in Part II, the gross features of the adiabatically forced easterly wave vertical motion field account for the varying relationships between easterly wave phase and convection over Africa noted in many previous studies. While these results do not necessarily address the mechanisms responsible for the initiation of AEWs, recent studies have indicated that convective initiation over the highland regions of Sudan may be important as seed disturbances (Berry and Thorncroft 2005; Mekonnen et al. 2006). The large spatial scale of the waves and their extension across the equator and outside the Tropics also leaves open the possibility that the waves could be initiated by extratropical forcing or other equatorial wave modes. The relative insensitivity of AEW structure to large changes in the basic-state circulation found by Part II, along with the observed large interannual variability in AEW activity argues for a strong dependence on initiation mechanisms to explain such variability.

Another interpretation of the results in the previous section is that the convection within AEWs is initiated by dynamical forcing, which induces vertical motion at low levels, which then couples the wave to deeper convection as it matures. This might help explain the two-tiered vertical motion structure in Fig. 9a, with the lower-level upward motion consistent with the maximum level of dynamical forcing, and the upper-level signal at around 300 hPa due to convective heating, as in other observed equatorial waves (e.g., Kiladis et al. 2005, and references therein).

In addition to further documentation of the dynamics of AEWs, it will be important to explore in detail in future studies how AEW variability is linked to lower-frequency rainfall variability over West Africa. For example, it is known that wet years in the Sahel tend to be

associated with a weaker and more poleward located AEJ, and dry years with a stronger and more equatorward AEJ (e.g., Newell and Kidson 1984; Grist and Nicholson 2001). Grist (2002) also found that wet years over the Sahel appeared to be accompanied by more AEW activity, although the direction of causality; that is, whether the basic state modulates AEWs, or vice versa, has not been established. West African rainfall can also vary significantly on intraseasonal time scales (e.g., Janicot and Sultan 2001; Mounier and Janicot 2004). However, little is known about the dynamics of such variability, its predictability, and its relationship to the AEJ and AEWs. The role of the MJO (e.g., Matthews 2004) and other equatorial waves along with hemispheric-scale teleconnections (e.g., Sultan et al. 2003) need to be further explored. Further elucidation of the factors governing AEW genesis and growth, and their relationship to the basic state will be a focus of our future work as well as the African Monsoon Multidisciplinary Analysis (AMMA) research and field program.

*Acknowledgments.* We thank Dan Keyser and Adam Sobel for valuable discussions concerning the dynamical arguments used in this study. Comments by three anonymous reviewers greatly helped to improve the manuscript. GNK was supported by NOAA's OGP under Grant GC05-156, CDT by NSF under ATM-0138290, and NMJH by the Centre National de la Recherche Scientifique (CNRS), France.

## APPENDIX

### Q Vector Calculation

In this study we are interested in the anomalous adiabatic forcing due to AEW perturbations propagating through a basic state (i.e.,  $\mathbf{Q}'$ ). This forcing could be approximated through centered differencing of the terms in Eqs. (1) and (2), using regressed perturbations, for example,

$$Q'_1 \approx -\frac{R}{p} \left( \frac{\partial u'}{\partial x} \frac{\partial \bar{T}}{\partial x} + \frac{\partial v'}{\partial x} \frac{\partial \bar{T}}{\partial y} + \frac{\partial \bar{u}}{\partial x} \frac{\partial T'}{\partial x} + \frac{\partial \bar{v}}{\partial x} \frac{\partial T'}{\partial y} + \frac{\partial u'}{\partial x} \frac{\partial T'}{\partial x} + \frac{\partial v'}{\partial x} \frac{\partial T'}{\partial y} \right), \quad (\text{A1})$$

$$Q'_2 \approx -\frac{R}{p} \left( \frac{\partial u'}{\partial y} \frac{\partial \bar{T}}{\partial x} + \frac{\partial v'}{\partial y} \frac{\partial \bar{T}}{\partial y} + \frac{\partial \bar{u}}{\partial y} \frac{\partial T'}{\partial x} + \frac{\partial \bar{v}}{\partial y} \frac{\partial T'}{\partial y} + \frac{\partial u'}{\partial y} \frac{\partial T'}{\partial x} + \frac{\partial v'}{\partial y} \frac{\partial T'}{\partial y} \right), \quad (\text{A2})$$

where  $Q_1$  is the  $x$  component and  $Q_2$  the  $y$  component, and the overbars represent long-term (1979–93) June–September means and the primes filtered deviations from those means. However, Eqs. (A1) and (A2) include only products between separately regressed perturbations, and not cross products that would be associated with the interaction between AEWs and other frequencies. Instead we calculate the total  $\mathbf{Q}$  vector using daily data according to Eqs. (1) and (2), then project these values onto TD-filtered OLR as was done for rest of the perturbation fields shown in this paper.

The vertical motion is proportional to the divergence of  $\mathbf{Q}$  (Hoskins et al. 1978);  $\nabla \cdot \mathbf{Q}'$  could be calculated directly using the perturbation form of Eqs. (1) and (2) by using centered differences, however, this results in significant numerical smoothing introduced by taking derivatives of products. Alternatively, it can be shown that

$$\frac{p}{R} \nabla \cdot \mathbf{Q} = \frac{\partial T}{\partial x} \frac{\partial \zeta}{\partial y} - \frac{\partial T}{\partial y} \frac{\partial \zeta}{\partial x} + \frac{\partial^2 \psi}{\partial x \partial y} \left( \frac{\partial^2 T}{\partial x^2} - \frac{\partial^2 T}{\partial y^2} \right) - \frac{\partial^2 T}{\partial x \partial y} \left( \frac{\partial^2 \psi}{\partial x^2} - \frac{\partial^2 \psi}{\partial y^2} \right), \quad (\text{A3})$$

which is consistent with the use of the rotational wind to calculate the  $\mathbf{Q}$  vector in Eqs. (1) and (2). As with the  $\mathbf{Q}$  vector calculation, the total  $\nabla \cdot \mathbf{Q}$  was calculated using Eq. (A3) on a daily basis, then projected onto TD-filtered OLR. Equation (A3) can also be decomposed into its perturbation form corresponding to Eqs. (A1) and (A2) using the basic state and perturbation vorticity and temperature.

Examination of the individual terms of Eqs. (A1) and (A2) reveals that the perturbation advection of the mean temperature field [the first two terms on the rhs of (A1) and (A2)], along with the first two terms on the rhs of the linearized version of (A3) (i.e., the Jacobian of perturbation vorticity versus mean temperature) account for virtually the entire pattern in Fig. 14. It turns out that the bulk of this signal is accounted for by terms involving the meridional gradient of mean temperature; that is,

$$Q'_1 \approx -\frac{R}{p} \left( \frac{\partial v'}{\partial x} \frac{\partial \bar{T}}{\partial y} \right), \quad (\text{A4})$$

$$Q'_2 \approx -\frac{R}{p} \left( \frac{\partial v'}{\partial y} \frac{\partial \bar{T}}{\partial y} \right), \quad (\text{A5})$$

$$\frac{p}{R} \nabla \cdot \mathbf{Q}' \approx -\frac{\partial \bar{T}}{\partial y} \frac{\partial \zeta'}{\partial x}, \quad (\text{A6})$$

representing the effect of perturbation vorticity advection by the mean thermal wind in the zonal direction.

## REFERENCES

- Albignat, J. P., and R. J. Reed, 1980: The origin of African wave disturbances during Phase III of GATE. *Mon. Wea. Rev.*, **108**, 1827–1839.
- Avila, L. A., and R. J. Pasch, 1992: Atlantic tropical systems of 1991. *Mon. Wea. Rev.*, **120**, 2688–2696.
- Berry, G., and C. D. Thorncroft, 2005: Case study of an intense African easterly wave. *Mon. Wea. Rev.*, **133**, 752–766.
- Burpee, R. W., 1972: The origin and structure of easterly waves in the lower troposphere of North Africa. *J. Atmos. Sci.*, **29**, 77–90.
- , 1974: Characteristics of North African easterly waves during the summers of 1968 and 1969. *J. Atmos. Sci.*, **31**, 1556–1570.
- , 1975: Some features of synoptic-scale waves based on a compositing analysis of GATE data. *Mon. Wea. Rev.*, **103**, 921–925.
- Carlson, T. N., 1969: Synoptic histories of three African disturbances that developed into Atlantic hurricanes. *Mon. Wea. Rev.*, **97**, 256–276.
- Céron, J.-P., and J. F. Guérémy, 1999: Validation of space-time variability of African easterly waves simulated by the CNRM GCM. *J. Climate*, **12**, 2831–2855.
- Davies-Jones, R., 1991: The frontogenetical forcing of secondary circulations. Part I: The duality and generalization of the Q vector. *J. Atmos. Sci.*, **48**, 497–509.
- Diedhiou, A., S. Janicot, S. Viltard, and H. Laurent, 1999: Easterly wave regimes and associated convection over West Africa and the tropical Atlantic: Results from NCEP/NCAR and ECMWF reanalyses. *Climate Dyn.*, **15**, 795–822.
- Druyan, L. M., M. P. Lonergan, and J. Cohen, 1997: Case studies of African wave disturbances in gridded analyses. *Mon. Wea. Rev.*, **125**, 2520–2530.
- Duvel, J. P., 1990: Convection over tropical Africa and the Atlantic Ocean during northern summer. Part II: Modulation by easterly waves. *Mon. Wea. Rev.*, **118**, 1855–1868.
- Fink, A. H., and A. Reiner, 2003: Spatiotemporal variability of the relation between African Easterly Jets and West African Squall lines in 1998 and 1999. *J. Geophys. Res.*, **108**, 4332, doi:10.1029/2002JD002816.
- , D. G. Vincent, P. M. Reiner, and P. Speth, 2004: Mean state and wave disturbances during Phases I, II, and III of GATE based on ERA-40. *Mon. Wea. Rev.*, **132**, 1661–1683.
- Frank, N. L., 1969: The “inverted v” cloud pattern—An easterly wave? *Mon. Wea. Rev.*, **97**, 130–140.
- , 1970: Atlantic tropical systems of 1969. *Mon. Wea. Rev.*, **98**, 307–314.
- Fyfe, J. C., 1999: Climate simulations of African easterly waves. *J. Climate*, **12**, 1747–1769.
- Gamache, J. F., and R. A. Houze, 1985: Further analysis of the composite wind and thermodynamic structure of the 12 September GATE squall line. *Mon. Wea. Rev.*, **113**, 1241–1259.
- Grist, J. P., 2002: Easterly waves over Africa. Part I: The seasonal cycle and contrasts between wet and dry years. *Mon. Wea. Rev.*, **130**, 197–211.
- , and S. E. Nicholson, 2001: A study of the dynamic factors influencing the rainfall variability in the West African Sahel. *J. Climate*, **14**, 1337–1359.
- Gu, G., R. F. Adler, G. J. Huffman, and S. Curtis, 2003: Summer synoptic-scale waves over West Africa observed by TRMM. *Geophys. Res. Lett.*, **30**, 1729, doi:10.1029/2003GL017402.
- , —, —, and —, 2004: African easterly waves and their association with precipitation. *J. Geophys. Res.*, **109**, D04101, doi:10.1029/2003JD003967.
- Haertel, P. T., and G. N. Kiladis, 2004: Dynamics of 2-day equatorial disturbances. *J. Atmos. Sci.*, **61**, 2707–2721.
- Hall, N. M. J., G. N. Kiladis, and C. D. Thorncroft, 2006: Three-dimensional structure of African easterly waves. Part II: Dynamical modes. *J. Atmos. Sci.*, **63**, 2231–2245.
- Hodges, K. I., and C. D. Thorncroft, 1997: Distribution and statistics of African mesoscale convective weather systems based on the ISCCP Meteosat imagery. *Mon. Wea. Rev.*, **125**, 2821–2837.
- , B. J. Hoskins, J. Boyle, and C. D. Thorncroft, 2003: A comparison of recent reanalysis datasets using objective feature tracking: Storm tracks and tropical easterly waves. *Mon. Wea. Rev.*, **131**, 2012–2037.
- Holton, J. R., 2004: *An Introduction to Dynamic Meteorology*. 4th ed. Elsevier Academic Press, 535 pp.
- Hoskins, B. J., I. Draghici, and H. C. Davies, 1978: A new look at the  $\omega$ -equation. *Quart. J. Roy. Meteor. Soc.*, **104**, 31–38.
- Hsieh, J.-H., and K. H. Cook, 2005: Generation of African easterly wave disturbances: Relationship to the African easterly jet. *Mon. Wea. Rev.*, **133**, 1311–1327.
- Janicot, S., and B. Sultan, 2001: Intraseasonal modulation of convection in the West African monsoon. *Geophys. Res. Lett.*, **28**, 523–526.
- Jenkins, M. A., and H.-R. Cho, 1991: An observational study of the first-order vorticity dynamics in a tropical easterly wave. *J. Atmos. Sci.*, **48**, 965–975.
- Kiladis, G. N., and M. Wheeler, 1995: Horizontal and vertical structure of observed tropospheric equatorial Rossby waves. *J. Geophys. Res.*, **100**, 22 981–22 997.
- , K. H. Straub, and P. T. Haertel, 2005: Zonal and vertical structure of the Madden–Julian Oscillation. *J. Atmos. Sci.*, **62**, 2790–2809.
- Lafore, J.-P., and M. W. Moncrieff, 1989: A numerical investigation of the organization and interaction of the convective and stratiform regions of tropical squall lines. *J. Atmos. Sci.*, **46**, 521–544.
- Landsea, C. W., G. D. Bell, W. M. Gray, and S. B. Goldenberg, 1998: The extremely active 1995 Atlantic hurricane season: Environmental conditions and verification of seasonal forecasts. *Mon. Wea. Rev.*, **126**, 1174–1193.
- Machado, L. A. T., J.-P. Duvel, and M. Desbois, 1993: Diurnal variations and modulation by easterly waves of the size distribution of convective cloud clusters over West Africa and the Atlantic Ocean. *Mon. Wea. Rev.*, **121**, 37–49.
- Madden, R., and P. Julian, 1994: Observations of the 40–50-day tropical oscillation—A review. *Mon. Wea. Rev.*, **122**, 814–837.
- Mallet, I., J.-P. Cammas, P. Mascart, and P. Bechtold, 1999: Effects of cloud diabatic heating on the early development of the FASTEX IOP-17 cyclone. *Quart. J. Roy. Meteor. Soc.*, **125**, 3439–3467.
- Mathon, V., and H. Laurent, 2001: Life cycle of Sahelian mesoscale convective cloud systems. *Quart. J. Roy. Meteor. Soc.*, **127**, 377–406.
- Matsuno, T., 1966: Quasi-geostrophic motions in the equatorial area. *J. Meteor. Soc. Japan*, **44**, 25–43.
- Matthews, A. J., 2004: Intraseasonal variability over tropical Africa during northern summer. *J. Climate*, **17**, 2427–2440.
- Mekonnen, A., C. D. Thorncroft, and A. R. Aiyyer, 2006: Analy-

- sis of convection and its association with African easterly waves. *J. Climate*, in press.
- Mounier, F., and S. Janicot, 2004: Evidence of two independent modes of convection at intraseasonal timescale in the West African summer monsoon. *Geophys. Res. Lett.*, **31**, L16116, doi:10.1029/2004GL020665.
- Newell, R. E., and J. W. Kidson, 1984: African mean wind changes between Sahelian wet and dry periods. *J. Climatol.*, **4**, 1–7.
- Nitta, T., 1978: A diagnostic study of interaction of cumulus updrafts and downdrafts with large-scale motions in GATE. *J. Meteor. Soc. Japan*, **56**, 232–242.
- , Y. Nakagomi, Y. Suzuki, N. Hasegawa, and A. Kadokura, 1985: Global analysis of the lower tropospheric disturbances in the tropics during the northern summer of the FGGE year. Part I. Global features of the disturbances. *J. Meteor. Soc. Japan*, **63**, 1–19.
- Norquist, D. C., E. E. Recker, and R. J. Reed, 1977: The energetics of African wave disturbances as observed during Phase III of GATE. *Mon. Wea. Rev.*, **105**, 334–342.
- Payne, S. W., and M. M. McGarry, 1977: The relationship of satellite inferred convective activity to easterly waves over West Africa and the adjacent ocean during phase III of GATE. *Mon. Wea. Rev.*, **105**, 414–420.
- Petersen, W. A., R. Cifelli, D. J. Boccippio, S. A. Rutledge, and C. Fairall, 2003: Convection and easterly wave structures observed in the eastern Pacific warm pool during EPIC-2001. *J. Atmos. Sci.*, **60**, 1754–1773.
- Pytharoulis, I., and C. D. Thorncroft, 1999: The low-level structure of African easterly waves in 1995. *Mon. Wea. Rev.*, **127**, 2266–2280.
- Reed, R. J., and E. E. Recker, 1971: Structure and properties of synoptic-scale wave disturbances in the equatorial western Pacific. *J. Atmos. Sci.*, **28**, 1117–1133.
- , D. C. Norquist, and E. E. Recker, 1977: The structure and properties of African wave disturbances as observed during Phase III of GATE. *Mon. Wea. Rev.*, **105**, 317–333.
- , E. Klinker, and A. Hollingsworth, 1988: The structure and characteristics of African easterly wave disturbances determined from ECMWF operational analysis/forecast system. *Meteor. Atmos. Phys.*, **38**, 22–33.
- Roca, R., J.-P. Lafore, C. Piriou, and J.-L. Redelsperger, 2005: Extratropical dry-air intrusions into the West African monsoon midtroposphere: An important factor for the convective activity over the Sahel. *J. Atmos. Sci.*, **62**, 390–407.
- Roundy, P. E., and W. M. Frank, 2004: A climatology of waves in the equatorial region. *J. Atmos. Sci.*, **61**, 2105–2132.
- Rowell, D. P., and J. R. Milford, 1993: On the generation of African squall lines. *J. Climate*, **6**, 1181–1193.
- Serra, Y. L., and R. A. Houze, 2002: Observations of variability on synoptic timescales in the east Pacific ITCZ. *J. Atmos. Sci.*, **59**, 1723–1743.
- Shapiro, L. J., 1978: The vorticity budget of a composite African tropical wave disturbance. *Mon. Wea. Rev.*, **106**, 806–817.
- Straub, K. H., and G. N. Kiladis, 2002: Observations of a convectively coupled Kelvin wave in the eastern Pacific ITCZ. *J. Atmos. Sci.*, **59**, 30–53.
- Sultan, B., S. Janicot, and A. Diedhiou, 2003: The West African monsoon dynamics. Part I: Documentation of intraseasonal variability. *J. Climate*, **16**, 3389–3406.
- Takayabu, Y. N., 1994: Large-scale cloud disturbances associated with equatorial waves. Part I: Spectral features of the cloud disturbances. *J. Meteor. Soc. Japan*, **72**, 433–448.
- , and T. S. Nitta, 1993: 3–5 day-period disturbances coupled with convection over the tropical Pacific Ocean. *J. Meteor. Soc. Japan*, **71**, 221–246.
- Thompson, R. M., Jr., S. W. Payne, E. E. Recker, and R. J. Reed, 1979: Structure and properties of synoptic-scale wave disturbances in the Intertropical Convergence Zone of the eastern Atlantic. *J. Atmos. Sci.*, **36**, 53–72.
- Thorncroft, C. D., 1995: An idealized study of African easterly waves. Part III: More realistic basic states. *Quart. J. Roy. Meteor. Soc.*, **121**, 1589–1614.
- , and M. Blackburn, 1999: Maintenance of the African easterly jet. *Quart. J. Roy. Meteor. Soc.*, **125**, 763–786.
- , and K. I. Hodges, 2001: African easterly wave variability and its relationship to Atlantic tropical cyclone activity. *J. Climate*, **14**, 1166–1179.
- , and B. J. Hoskins, 1994: An idealized study of African easterly waves. Part I: A linear view. *Quart. J. Roy. Meteor. Soc.*, **120**, 953–982.
- Viltard, A., P. de Felice, and J. Oubuih, 1997: Comparison of the African and the 6–9 day wave-like disturbance patterns over West Africa and the tropical Atlantic during summer 1985. *Meteor. Atmos. Phys.*, **62**, 91–99.
- Wheeler, M., and G. N. Kiladis, 1999: Convectively coupled equatorial waves: Analysis of clouds in the wavenumber-frequency domain. *J. Atmos. Sci.*, **56**, 374–399.
- , —, and P. J. Webster, 2000: Large-scale dynamical fields associated with convectively coupled equatorial waves. *J. Atmos. Sci.*, **57**, 613–640.